Biosensors and Bioelectronics 143 (2019) 111599

Contents lists available at ScienceDirect

Biosensors and Bioelectronics

journal homepage: www.elsevier.com/locate/bios

Interference-free and high precision biosensor based on surface enhanced Raman spectroscopy integrated with surface molecularly imprinted polymer technology for tumor biomarker detection in human blood

Xueliang Lin[a], Yunyi Wang[a], Lingna Wang[b], Yudong Lu[c], Jin Li[d], Dechan Lu[c], Ting Zhou[c], Zufang Huang[a], Jun Huang[e], Huifang Huang[e], Sufang Qiu[f], Rong Chen[a], Duo Lin[g,*], Shangyuan Feng[a,**]

[a] Key Laboratory of OptoElectronic Science and Technology for Medicine, Ministry of Education, Fujian Provincial Key Laboratory for Photonics Technology, Digital Fujian Internet-of-Things Laboratory of Environment Monitoring, Fujian Normal University, Fuzhou, 350007, PR China
[b] Fujian Pien Tze Huang Cosmetics Co., Ltd, Zhangzhou, 363000, PR China
[c] Fujian Key Laboratory of Polymer Materials, College of Chemistry and Materials Science, Fujian Normal University, Fuzhou, 350007, PR China
[d] State Key Laboratory of Physical Chemistry of Solid Surfaces, College of Chemistry and Chemical Engineering, Collaborative Innovation Center of Chemistry for Energy Materials (iChEM), Xiamen University, Xiamen, 361005, PR China
[e] The Central Laboratory, Clinical Laboratory, Fujian Medical University Union Hospital, Fuzhou, 350001, PR China
[f] Department of Radiation Oncology, Fujian Provincial Cancer Hospital, Fujian Medical University Cancer Hospital, Fujian Provincial Key Laboratory of Translational Cancer Medicine, Fuzhou, 350014, PR China
[g] College of Integrated Traditional Chinese and Western Medicine, Fujian University of Traditional Chinese Medicine, Fuzhou, 350122, PR China

ARTICLE INFO

Keywords:
Surface enhanced Raman scattering
Surface molecularly imprinted polymer
Nanoparticles
Raman reporter
CEA
Quantitative detection

ABSTRACT

The reliable quantitative analysis of tumor biomarkers in circulating blood is crucial for cancer early screening, therapy monitoring and prognostic prediction. Herein, a novel biosensor combing surface-enhanced Raman spectroscopy (SERS) and surface molecularly imprinted polymer (SMIP) technology was developed for quantitative detection of carcinoembryonic antigen (CEA) that is closely related to several common cancers. Owing to the use of SMIP, recognition sites with high affinity to the target of interest can be well imprinted on the surface of SERS substrate, leading to a more stable and specific capture ability. In addition, two layers of core-shell nanoparticles were integrated to this SERS substrate to form highly efficient electromagnetic enhancement for SERS measurement via the generation of lots of "hot spot". Besides, a unique Raman reporter (C≡C) with silent Raman signals at 2024 cm^{-1} was capsulated in the nanoparticles to avoid the optical noises originating from endogenous molecules at fingerprint region (300-1800 cm^{-1}). Meanwhile, we employed an internal standard molecular (C≡N) to real time correct the fluctuating signals of Raman reporter when performing the quantitative analysis. Due to these features, a limit of detection (LOD) of 0.064 pg mL^{-1} with the detection range of 0.1 pg mL^{-1} - 10 μg mL^{-1} can be achieved by this assay. Excitingly, this technology even showed wonderful performances for CEA detection in real blood from cancer patients, demonstrating great potential for biomarker-based cancer screening.

1. Introduction

According to Cancer Statistics (2016), cancer has been the second leading cause of death in developed countries (Siegel et al., 2016) and there are about 2.8 million people dying of cancer in China (Chen et al., 2016a). Early screening and effective prognosis monitoring of cancers can greatly improve patients' five-year survival rate (Lee et al., 2015), which mainly relies on the ultrasensitive and reliable quantitative detection of cancer biomarkers in tumor tissue and body fluid (blood, saliva and urine) samples. Some of these cancer biomarkers have been widely used for routine cancer screening in clinical practice (Hanash et al., 2008). For example, carcinoembryonic antigen (CEA), one of glycoproteins, has been employed as a broad spectrum of traditional tumor marker, with the ability of reflecting the presence of multiple

* Corresponding author.
** Corresponding author.
E-mail addresses: linduo1986@163.com (D. Lin), syfeng@fjnu.edu.cn (S. Feng).

https://doi.org/10.1016/j.bios.2019.111599
Received 26 June 2019; Received in revised form 6 August 2019; Accepted 13 August 2019
Available online 21 August 2019
0956-5663/

cancers, such as colorectal, breast, ovarian, lung, gastric, bladder and pancreatic cancer (Han et al., 2018; Konishi et al., 2018).

Currently, traditional methods for detecting CEA include enzyme-linked immunosorbent assay (ELISA) (Liu et al., 2015), radioimmunoassay (RIA) (Liu et al., 2016), fluorescence polarization immunoassay (Khang et al., 2017), automated immunoassay (Lumachi et al., 2016), etc. Although effective, these methods require the use of corresponding antibody-antibody or antigen-conjugated labels, and these labels are associated with some limitations. On the other hand, these techniques fail to meet all the expectations of modern biomedical science because they are time consuming, have relatively poor detection limit, and sometimes require special environments that are far from biological conditions (Alvarez-Puebla and Liz-Marzán, 2010). Moreover, radioisotopes may cause health hazards, and many fluorescence and chemiluminescence probes are disturbed by the test environment (Tu et al., 2016). Thus, rapid, ultrasensitive and specific detection methods that can overcome the above drawbacks are highly needed.

In the last decade, surface-enhanced Raman spectroscopy (SERS) based on nano-optical technology has attracted significant attentions due to its ultrasensitive detection ability at even single molecule level, providing a novel and powerful method for biomedical applications, especially for the detection of various cancer biomarkers (Feng et al., 2017; Gao et al., 2018; Pang et al., 2019; Wang et al., 2017; Zong et al., 2018). Our team also reported a urinary modified nucleoside detection method based on SERS for gastric cancer and breast cancer detection (Lin et al., 2019b). In addition, we employed SERS to detect low concentrations of nasopharyngeal cancer-related DNA, and the results demonstrated that SERS technology could provide a reliable and ultrasensitive method for cancer biomarkers detection (Lin et al., 2019a). In order to further improve the efficiency of immuno-SERS assay for detecting the targets, a surface molecularly imprinted polymer (SMIP) technology recently was integrated with SERS to develop a more powerful detection strategy (SMIP-SERS), owing to the better antibody-like binding properties or enzyme-like activities generated by templated polymerization. Besides, this SMIP-SERS assay is easy to prepare and cost-efficient, presenting significant advantages over traditional immune-SERS assay. Recently, Liu zhen et al. reported that SMIP based SERS immunoassays was used for determination of cancer biomarkers such as AFP, erythropoietin, alkaline, survivin and sialic acid, indicating that the SMIP-SERS analysis provided a promising potential tool for quantitative detected cancer biomarkers in complex samples (Tu et al., 2016; Ye et al., 2015). Although sensitive and promising, these works still suffer from some limitations. First, the signals of Raman probe used in those works lie on the fingerprint region (300-1800 cm^{-1}) and thus are greatly easy to be interfered by the Raman signals from endogenous biomolecules. Second, the intensity of SERS peak used for quantitative detection often exist unexpected fluctuation due to the variation of laser power and external environment. Both of factors will affect the eventual accuracy of quantitative detection, significantly limiting the further application of this method for the detection of complex biological samples.

In light of these challenges, a specially designed SMIP-SERS detection platform fabricated with interference-free Raman probes and stable internal standard (IS) was developed in this work for quantitative detection of CEA. The Raman signals of the probes (C≡C) used here located in a silent region (1800-2300 cm^{-1}), thus could avoid the overlap with the signals from endogenous molecules. Besides, a IS molecule (C≡N) was employed to real time correct the intensity of Raman probes for achieving a stable and accurate concentration detection by the use of intensity ratio of Raman probe and IS peaks. Furthermore, this novel method was applied for real blood samples detection to evaluate its feasibility for potential clinical application.

2. Experimental method section

2.1. Materials and instruments

Dopamine hydrochloride, tris (hydroxymethyl) aminomethane (Tris) and ammonium persulfate (APS) were purchased from J & K Biochemistry Co., Ltd (Beijing, China). Trisodium citrate, silver nitrate (99.99%), L-ascorbic acid (98%), 4-mercaptophenylboronic acid (MPB), 4-aminothiophenol (PATP) and sodium dodecyl sulfate (SDS) were purchased from Aladin Co., Ltd (Shanghai, China) and used as received. m-Aminophenylboronic acid monohydrate (APBA) was purchased from MACKLIN Co., Ltd (Shanghai, China). Bovine serum albumin (BSA), sodium hydroxide (NaOH), hydrochloric acid (HCl), glacial acetic acid (HAc), phosphate-buffered saline (PBS), dimethyl sulfoxide (DMSO) and hydrogen tetrachloroauratehydrate ($HAuCl_4 \cdot 4H_2O$) were purchased from Sinopharm Chemical Reagent Co., Ltd (Beijing, China) and used directly. 4-Mercaptobenzonitrile (MB, 98%) was purchased from Nanjing Sheng Sal Chemical Co., Ltd (Nanjing, China). Ethynylbenzene (EB) was purchased from Aladin Co., Ltd (Shanghai, China) and was used without further purification. Ultrapure water (resistivity of 18.2 MΩ cm) purified with Milli-Q system was used throughout the work. All solvents unless specified were obtained from Sigma-Aldrich. CEA antibody (CEA Ab) and CEA antigen (CEA) were purchased from BBI Life Sciences Co., Ltd (Shanghai, China). Human AFP antigen (AFP) was purchased from Shanghai Linc-Bio Science Co., Ltd (Shanghai, China). Glucose was purchased from GuangzhouXilong Scientific Co., Ltd (Guangzhou, China). Gold coated microarray substrates (75 mm × 25 mm, GCMS) were purchased from Thermo scientific Co., Ltd.

UV–Vis spectra were obtained using Lambda 950 (PerkinElmer, USA). The dynamic light scattering (DLS) and the zeta potential measurements were performed on a Malvern Zetasizer NanoZ (Malvern Panalytical, UK). Transmission electron microscopy (TEM) and the scanning transmission electron microscopy (STEM) images were obtained using a Tecnai-G20 (FEI, USA). Scanning electron microscopy (SEM) images were obtained using a SU 8010 (Hitachi, Japan). The high-resolution SERS spectra were recorded using a Renishaw inVia Raman microscope (Renishaw plc, UK) equipped with 785 nm laser sources. The software package WiRE 3.4 (Renishaw) was employed for Raman spectral acquisition and analysis. Before measurement, the Raman spectrometer was calibrated using the standard Raman spectrum of silicon, whose first order Raman peak was centered at 520 cm^{-1}. The SERS spectrum was collected from five random points on each of SMIP arrays. All spectra were presented after the removal of fluorescence from the original SERS data using a polynomial multipoint fitting function.

2.2. Design of the biosensor

The design of biosensor mainly includes four parts. 1) We synthesized Au@EB@PDA NPs with a Raman probe embedded to recognize and indicate CEA (Fig. 1A). 2) We constructed a unique Au@Ag NPs with an IS embedded in the gap of core-shell nanostructure (Au@MB@Ag@PATP/MPB NPs, core-molecule-shell-molecule NPs, CMSM NPs) to real-time correct fluctuating signals of Raman probe (Fig. 1B). 3) With the use of SMIP technology, we prepared CMSM NPs based SERS substrate with highly specific and stable recognition sites to capture the CEA (Fig. 1C). 4) In the presence of CEA, strong signals of both Raman probe and IS in silent Raman region can be obtained using a unique sandwich structure. Finally, the intensity ratio based on Raman probe and IS can be used to quantify the concentrations of CEA (Fig. 1D). More details are described in following sections.

2.3. Preparation of Au nanoparticles (Au NPs)

Au NPs were prepared using the reduction method reported

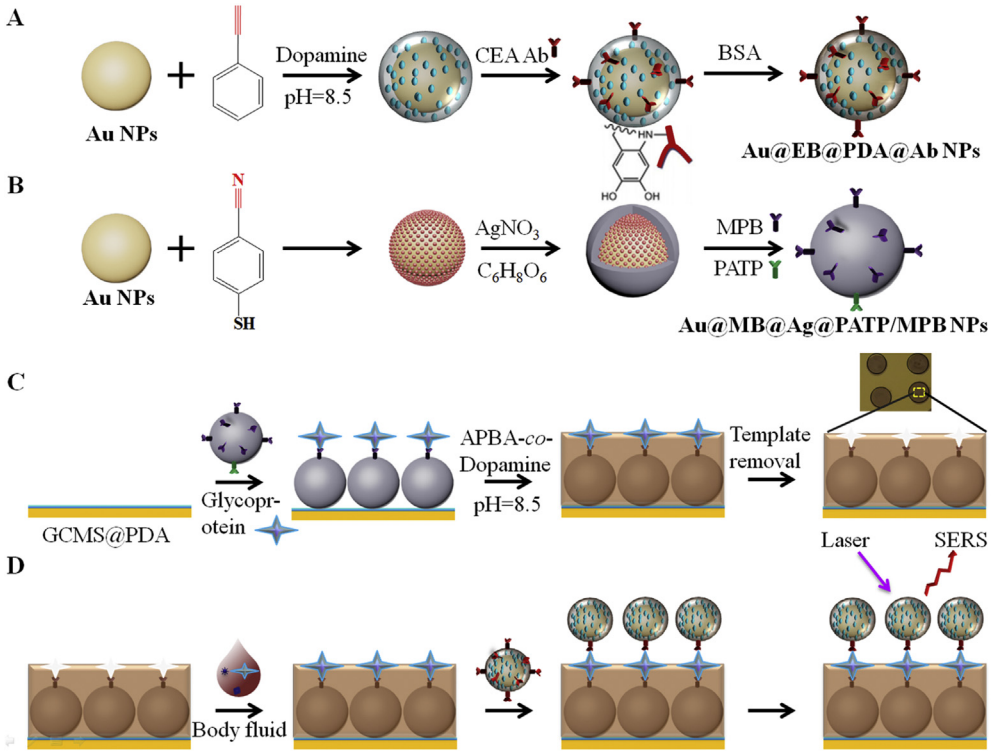

Fig. 1. (A) Schematic illustration of the fabrication process of polydopamine encapsulated SERS probes. The exposed dopaminequinone on the PDA shell reacts with the amine group on antibody via Michael addition reaction. (B) Schematic illustration of the Au@MB@Ag@PATP/MPB NPs. (C) Schematic illustration of preparing Boronate affinity-based glycoprotein imprinted arrays. (D) The SMIP-based SERS approach for the detection of glycoprotein.

according to the previous report by Grabar et al., (1995). Briefly, 1 mL of 100 mM $HAuCl_4$ was added into 99 mL of rolling boil water, with a final concentration of 1 mM, followed by boiling and vigorous stirring for an additional 2 min. Then, 1 mL of 1% wt sodium citrate was added into the vortex of the solution resulting in a color change from pale yellow to ruby-red. Boiling and stirring was continued for 15 min to ensure the formation of uniform quasi-spherical Au NPs, then the heat source was removed and cooled down to room temperature. The maximum absorption peak of prepared Au colloid was located at 526 nm and the colloidal concentration was determined to be 0.35 nM using UV–Vis spectroscopy (Fig. 2F(a)). Moreover, Au NPs sizes were represented with a mean diameter of 30 nm with the standard deviation of 3 nm by transmission electron microscopy (TEM) (Fig. 2A). This dynamic dispersion illustration showed the size distribution of Au NPs.

2.4. Preparation of EB-coded dopamine-assisted SERS nanotag

The method of preparing EB-coded SERS nanotag reported according to the previous report by Li et al., (2018). In brief, the EB was dissolved in DMSO to form 10 mM solutions. 100 μL of the EB solution was mixed with 5 mL of 0.1 mg mL^{-1} dopamine in Tris buffer (10 mM, pH 8.5) and 5 mL of Au NPs solutions. The mixture was stirred vigorously for 1 h. With the polymerization of dopamine to generate polydopamine (PDA), the reporter molecule was coated on the surface of Au NPs to produce SERS probes with high SNR. After that, the resulting solution was centrifuged at 8000 rpm for 10 min to remove the excess dopamine. Then Au@EB@PDA NPs were filtrated through syringe filters with cellulose acetate membranes with a pore size of 0.22 μm to avoid the aggregation. These nanotags were resuspended in 1 mL of ultrapure water and stored at 4 °C for further use. For antibody conjugation procedure, 2.5 μL of 1 mg mL^{-1} CEA Ab was added to 200 μL of Au@EB@PDA NPs colloid and incubated at 4 °C for 12 h. Then, 5 μL of 10 mg mL^{-1} BSA was added and incubated at 37 °C for 1 h to block unreacted catechol groups.

2.5. Preparation of CMSM NPs

CMSM NPs were prepared as the bottom of SMIP and the calibration signal source of Raman quantitative detection according to reported method with a slight modification (Shen et al., 2015). In brief, 10 mL of Au NPs colloidal solution was mixed with 10 μL of 10 mM aqueous MB solution (dissolved in DMSO) under magnetic stirring for 1 h to bind Au NPs-Raman reporter via Au–S bonds. Then, the Au@MB NPs colloid was centrifuged three times at 8000 rpm for 12 min, and the sediment was resuspended in 10 mL ultrapure water. After that, 2 mL of 0.1 M L-ascorbic acid solutions was added to the Au@MB NPs colloid under stirring. Afterward, 2.5 mL of 1 mM $AgNO_3$ solution was dropwise added by pipet while vigorously stirring the mixture. The resultant silver continuously grew on the surface of Au@MB NPs because of the reduction of $AgNO_3$ by L-ascorbic acid. After the color of the solution changed from pink to yellow-orange, the solution still needed to be stirred for 30 min. Then, the mixture was centrifuged three times and dispersed in 10 mL of ultrapure water. Next, 4 μL of 1 mM PATP and 30 μL of 10 mM MPB was added to the bimetal core-shell nanostructure solution and the mixed solution was stirred for 1 h at room temperature. Finally, the obtained CMSM NPs were stored at 4 °C for further use.

2.6. Preparation of CMSM NPs circular array coated GCMS

GCMS (75 mm × 25 mm) were cut into four equal pieces (18.75 mm × 25 mm). Then, the GCMS were cleaned by immersion in dehydrated alcohol with ultrasound for 15 min. Then, the GCMS were rinsed thoroughly with ultrapure water for three times and immersed in 10 mL of 0.1 mg mL^{-1} dopamine in Tris buffer (10 mM, pH 8.5) for 1 h. Because of the unique ability of PDA was capable of tightly attaching to virtually any surfaces, the GCMS@PDA was obtained and dried by nitrogen. Next, the GCMS@PDA was coated with above-prepared CMSM NPs. Briefly, 10 mL of CMSM NPs colloidal solution were centrifuged at 8000 rpm for 10 min, and the sediment was resuspended in 200 μL of ultrapure water. Then, 8 μL of CMSM NPs colloidal solution was dropped on the plate using a pipet to form a circular array and incubated in a wet chamber for 24 h. The targeting ligands (PATP) can be

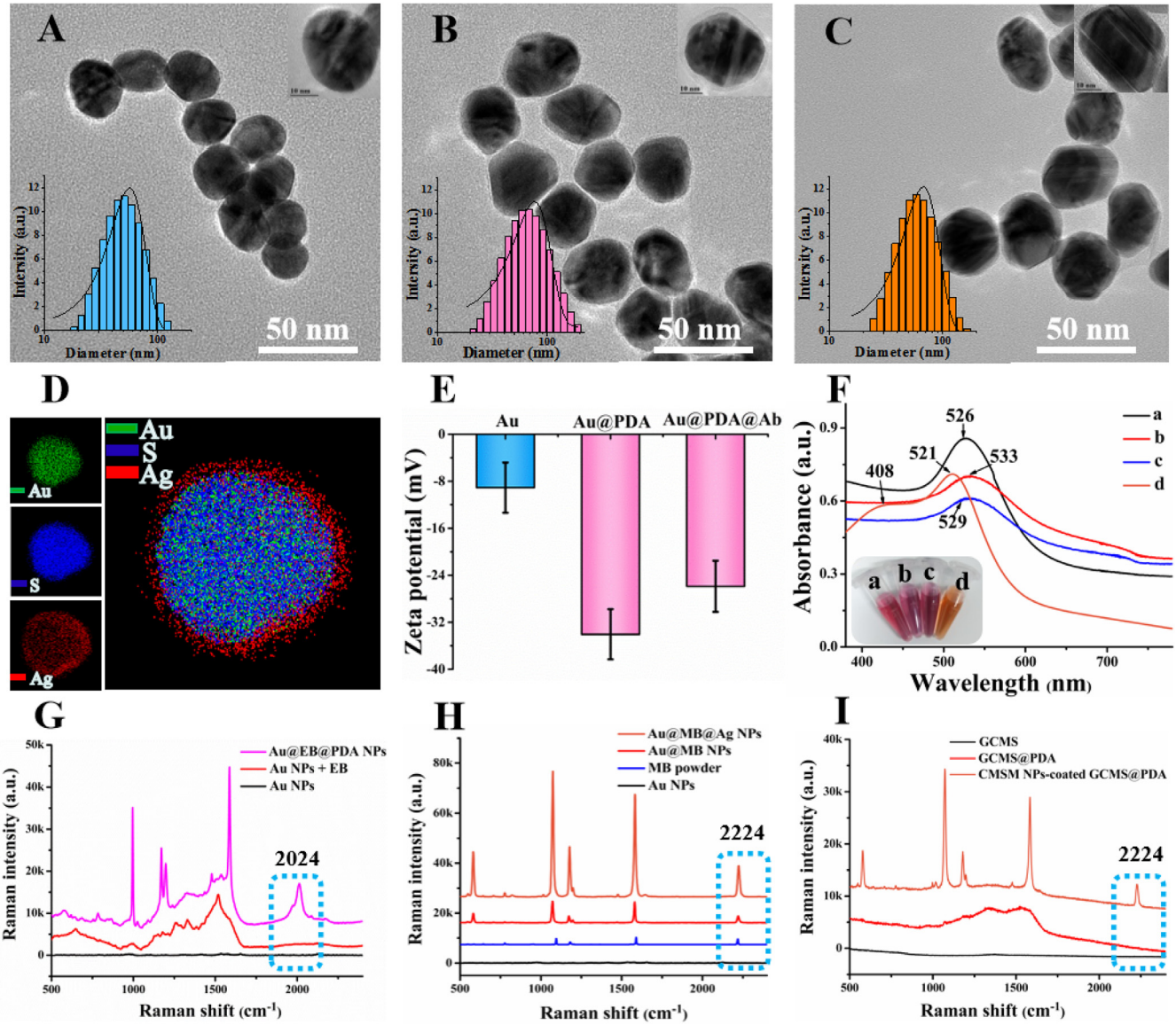

Fig. 2. (A) TEM image of Au NPs. Inset: hydrodynamic diameters of Au NPs. (B) TEM image of Au@PDA NPs. Inset: hydrodynamic diameters of Au@EB@PDA NPs. (C) TEM image of Au@MB@Ag NPs. Inset: hydrodynamic diameters of Au@MB@Ag NPs. (D) STEM images of the CMS NPs using the Au-M, S–K, and Ag-L signals. And the superimposed image of the STEM images of Au-M, Ag-L and S–K. (E) Zeta potentials of Au NPs, Au@EB@PDA NPs and those functionalized with CEA antibodies (Ag@EB@PDA@Ab NPs). (F) UV–Vis spectra of the Au NPs (a), Au@EB@PDA NPs (b), Au@MB NPs (c) and Au@MB@Ag NPs (d). (G) Raman spectra of Au NPs, Au NPs + EB (EB solution is added to Au NPs colloid with slow stirring for 1 h), Au@EB@PDA NPs. (H) Raman spectra of Au NPs, MB powder, Au@MB NPs, and Au@MB@Ag NPs. (I) Raman spectra of GCMS, GCMS@PDA, CMSM NPs-coated GCMS@PDA.

easily conjugated to the PDA outer surface via Michael addition through the exposed dopamine quinone. After that, the CMSM-coated GCMS@PDA was gently washed with water three times and dried with nitrogen.

2.7. Preparation of CEA-imprinted SMIP arrays

The molecular imprinting approach was slightly modified from the reported method called boronate affinity-based controllable oriented surface imprinting (Lv et al., 2016). The binding pH value was set to 7.4, which is beneficial to the binding between common phenylboronic acids and CEA glycoproteins. A 3 μL solution of 10 μg mL^{-1} CEA dissolved in PBS (pH 7.4) was added onto each spot of the CMSM-coated circular arrays. Then the circular arrays were incubated for 20 min in a humidity chamber to form a thin template layer followed by rinsing with PBS (pH 7.4) several times until no UV–Vis absorbance signal is detected at 280 and 218 nm. Then the template-anchored circular arrays were immersed in the aqueous mixture (the concentrations ratio of dopamine, APBA and APS are 2.0:1.6:1.2 mg mL^{-1}) at room temperature for 60 min. Finally, the arrays were soaked with 20 mL of 0.1 M HAc containing 10% SDS (wt/vol) solution in a 50 mL centrifuge tube to remove the template (Fig. 1C). The template elution time was then fixed to the optimal value. Moreover, compared with molecular imprinting, the processing procedure of the non-imprinted (NIP) arrays covered arrays was the same except that no template was immobilized onto the CMSM arrays. Finally, the imprinted plate can be stored in a dry and sealed tube at 4 °C for further use.

2.8. Preparation of serum samples

In the study, the serum samples were collected from 5 healthy volunteers and 3 colon cancer patients with confirmed clinical diagnosis from Fujian tumor hospital. The serum samples were collected according following processes. Firstly, 1 mL of serum was collected from

Table 1
Comparison of linear dynamic range and limit of detection between different approaches.

Method	Linear dynamic range	Limit of detection	Reference
DPV	0.001–80 ng mL^{-1}	0.2 pg mL^{-1}	Feng et al. (2016)
EIS	0.05–80 ng mL^{-1}	0.1 pg mL^{-1}	Zeng et al. (2015a)
SERS	1–50 ng mL^{-1}	100 pg mL^{-1}	Lin et al. (2016)
Fluorescence	0.02–50 ng mL^{-1}	5.6 pg mL^{-1}	Lin et al. (2017)
ELISA	0.1–20 ng mL^{-1}	30 pg mL^{-1}	Liu et al. (2015)
SMIP-SERS	0.0001–10000 ng mL^{-1}	0.064 pg mL^{-1}	This work

Table 2
Detection and recovery test of CEA in the human serum samples.

Samples	CEA concentration (ng mL^{-1})		
	Referenced method	Proposed method	Recovery (%)
1	< 0.2	0.925 ± 0.102	no value
2	1.42	1.44 ± 0.09	101.4%
3	1.88	1.85 ± 0.11	98.4%
4	3.50	3.72 ± 0.14	106.3%
5	4.14	4.19 ± 0.18	101.2%
6	10.16	10.05 ± 0.22	98.4%
7	112	118.15 ± 4.65	105.5%
8	325	341.50 ± 9.42	105%

each study subject between 7:00 and 8:00 a.m. after 12 h of overnight fasting. Prior to analysis each sample was first centrifuged at 3000 rpm for 10 min and the supernatant was collected and stored at −20 °C for further use. 200 μL of each serum sample were measured using commercial electochemiluminescent immunoassay (ECLIA) kits in hospital. The results were shown in Table 2. This work was approved by the local ethics committee (No. SQ2018-025-01), and informed consents were obtained from all participating subjects.

3. Results and discussion

3.1. Synthesis and characterization of SERS nanotags

To establish the PDA coating conditions, Au NPs were used as the plasmonic core due to their outstanding ability in enhancing SERS signals (Fig. 1A). Through a universal method for one-pot synthesis, a PDA shell of approximately 4.5 nm in thickness was coated onto the Au NPs (Au@EB@PDA NPs), as shown in the TEM micrograph (Fig. 2B). This dynamic dispersion illustration shows the size distribution of Au@EB@PDA NPs. The characteristic absorption profile of the Au NPs shifted from 526 to 533 nm (Fig. 2F(a) and (b)), likely due to the change of local dielectric environment induced by the PDA layer. DLS measurements revealed that the average hydrodynamic size of the Au NPs increased from 28.5 ± 2.3 to 37.3 ± 2.3 nm after PDA coating (Fig. 2B), and the surface charge measured as zeta potential also changed from −9.1 ± 4.2 to −34.0 ± 4.2 mV (Fig. 2E), further confirming successful PDA coating. Upon addition of CEA Ab, the average zeta potential of the Au@EB@PDA@Ab NPs dropped back to −25.9 ± 4.4 mV (Fig. 2E). These results indicated that the strong adhesion force between PDA and EB kept the encapsulated EB close to the surface Au NPs. Additionally, the Au@EB@PDA SERS nanotags with remarkable features discussed above were easy to prepare and highly reproducible of different batch (Fig. 3A). More importantly, the prepared Au@EB@PDA NPs showed a unique and narrow sharp band at 2024 cm^{-1} (Fig. 2G) in the Raman scattering silent region that normally refers to the range of 1800–2300 cm^{-1}. In order to evaluate the storage stability of Au@EB@PDA NPs, we measured the UV–Vis absorption and Raman signal for the same batch of Au@EB@PDA NPs within 7-day. As shown in Figs. S1A and B, the Au@EB@PDA NPs was stable throughout the 7-day storage time. As we known, sensitive SERS-based quantitative detection for biological samples mainly depends on the use of the Raman reporters with strong and distinct Raman signals to track and indicate the targets of interest. However, the Raman signals of most used Raman reporters locate in the range of 300–1800 cm^{-1}, which greatly overlaps with the Raman signals from endogenous molecules. Owing to this interference, the correlation between the Raman signals and the concentrations of target will be significantly affected, leading to an inevitably less reliable results for quantitative SERS assays, especially for the targets with an ultra-low concentration. Thus, it is necessary to explore a unique kind of Raman reporter, which allows us to observe the changes of Raman signals in an interference-free Raman region when performing the quantitative assays. Recently, researchers have developed a series of novel Raman reporters with signals at Raman scattering silent region to improve the efficiency of quantitative SERS assays. For example, sensitive sensing for glucose with the LOD of 100 μM could be achieved by a unique SERS detection platform functionalized with an alkyne group that exhibited a distinct Raman peak at 1996 cm^{-1} in a biological silent region (Kong et al., 2014). Besides, Hu's group also developed an alkyne-containing Raman reporters with band shift-tunable signals at (2100-2300 cm^{-1}), and successfully applied them for multiplex cellular imaging due to their super sensitivity and minimal optical interferences (Chen et al., 2016b). Inspired by these studies, we thus applied the alkynyl (C≡C) group with signals (2024 cm^{-1}) at Raman scattering silent region as a stable Raman probe for CEA sensing.

3.2. Synthesis and characterization of Au@MB@Ag NPs

Bimetallic core-shell nanostructures such as Au@Ag are regarded to be superior to the single metal in physical and chemical properties. In fact, Au@Ag nanostructure substrates have been widely investigated for SERS assays (Li et al., 2017; Tang et al., 2015; Zeng et al., 2015b). The Au@MB@Ag NPs (core-molecule-shell NPs, CMS NPs) were synthesized by one type of embedded Raman probe molecules shown in Fig. 1B. We chose Au NPs as the core to obtain a highly uniform core, silver as the shell to achieve the highest possible enhancement, and MB as the IS. The UV–Vis characteristic absorption peak of the Au@MB NPs is 529 nm (Fig. 2F(c)). MB can bind to the gold cores through Au–S bonds and the silver atoms can easily grow on the surface of Au@MB NPs because of the strong affinity of the cyan group and negatively charged Au NPs. TEM image (Fig. 2C) of the CMS NPs indicates that the CMS NPs are structurally uniform and a light silver shell surrounding the dark gold core can be clearly identified. The average diameter of the CMS NPs is about 40.1 ± 3.8 nm. This dynamic dispersion illustration shows the size distribution of Au@MB@Ag NPs. In addition, STEM mapping images clearly show the spatial distribution of the Au core, the Ag shell, and the embedded MB layer in this core-shell structure (Fig. 2D). The signals of element S cannot be found in outer Ag shell, indicating the Raman probe of MB is well embedded between the Au core and Ag shell. The UV–Vis characteristic absorption peaks of the CMS NPs are 408 and 521 nm (Fig. 2F(d)), which show the presence of silver shell and gold core, respectively. Excitingly, the Raman signal at 2224 cm^{-1} of MB is dramatically enhanced in the CMS NPs compared with Au@MB NPs, which can be attributed to more and stronger “hot-spots” generated by the gap between the Au core and the Ag shell (Fig. 2H). In this case, we propose that the MB might be an ideal internal reference for stable and accurately quantitative SERS analysis due to following reasons. (1) MB with a thiol (-SH) has only one binding site to the surface of Au NPs, and thus can be well embedded as a monomolecular layer between the silver layer and Au NPs; (2) This sandwich structure not only avoids the risk of dynamic replacement of this internal reference (MB) in complex environment, but also provides plenty of available surface sites for various functional modifications; (3) Similar to the EB molecule, the Raman signal of MB also locates in a silent region (2224 cm^{-1}), making it more suitable to be an internal reference without the interference from the Raman signals (300-

1800 cm^{-1}) of endogenous biomolecules. The above results show that we have successfully obtained these specially-designed CMS NPs. The preparation reproducibility of CMS NPs is an important factor for practical applications of this SERS substrate. Thus, we evaluate this property via UV–Vis absorption spectra and Raman spectra (Figs. S2A and B). Results show high preparation reproducibility for CMS NPs array can be achieved in this work.

3.3. Synthesis and characterization of CMSM NPs and CMSM NPs-coated GCMS

The stability of the CMSM NPs was also evaluated by continued absorption and Raman spectra measurement (Figs. S3A and B). These results confirm that the storage stability of CMSM NPs was significantly stable throughout the 7-day storage time. PATP, as targeting ligands, was used to hold CMSM NPs to the PDA coated GCMS via Michael Addition (Ahn, 2017). MPB ligands can be covalently and reversibly bound with cis-dihydroxyl groups of glycoproteins to form stable cyclic esters in alkaline aqueous solutions and enrich the target molecules (CEA) (Wang et al., 2014). When the surrounding pH value becomes acidic, borate esters will dissociate and separate the target molecules (CEA). Fig. 2I shows the pure GCMS has no Raman signal in the spectral region of 500–2400 cm^{-1}. When a layer of polydopamine coated on the GCMS (Lee et al., 2007), two characteristic Raman peaks at 1330 and 1540 cm^{-1} were observed. The targeting ligands on CMSM NPs can be easily conjugated to the PDA outer surface via Michael addition through the exposed dopamine quinone, forming a CMSM NPs-based SERS substrate (Ahn, 2017). The SEM image shows morphology of array formed by CMSM NPs, which demonstrates a uniform distribution of nanoparticles on the PDA surface (Fig. S4A). In addition, the SERS reproducibility of the IS signal was explored by recording 274 Raman spectra over an area of 200 μm (Fig. 3B). It can be observed that the Raman spectra of C≡N are highly reproducible and stable with the relative standard deviation (RSD) of as low as 9.95%. Therefore, we employed the CMSM NPs-coated GCMS as reliable substrates for following SMIP arrays. Further, the uniformity of 2D CMSM NPs array was validated by the Raman mapping using the intensity of peak at 2224 cm^{-1} (Fig. S5).

3.4. Preparation of CEA-imprinted arrays and optimization of elution time

In this study, 28-spot (7 × 4) SMIP arrays were used to evaluate the detection effect of SMIP–IS–SERS. The boronic acid-functionalized CMSM NPs-coated array was silvery grey, while the SMIP array was darker due to the presence of the poly layer (APBA-*co*-dopamine) on the array. SMIP arrays can be fabricated into any size of larger numbers of circular spots for immunosorbent assay through some slight technical modifications. The thickness-imprinting time relationship established according to the previous report by wang et al. ($y = 0.25 + 3.49\ x$, $R^2 = 0.95$, where y is in nm and x is in hour) (Wang et al., 2014). When the CEA-imprinting time at 1 h, the thickness of PDA coating over the CMSM NPs array is about 3.74 nm. We can clearly see the successful coating of the CMSM NPs on the GCMS and the successful preparation of CEA-imprinted arrays in Fig. S6. As we all know, the elution time of template molecules has an important influence on the subsequent CEA quantitative analysis. To determine the optimized template elution time, the SMIP arrays plate was immersed in SDS solution and oscillated in an oscillator for a series of time (20, 40, 60, 80, 100, 120, 140, 160 and 180 min) to measure the ultraviolet absorption intensity of the eluent, respectively. As shown in Fig. 3C, the UV–Vis absorption peak of template molecular eluent decreased significantly in the first 80 min, and then decreased slowly in 80–180 min, until there was no absorption peak in 180 min. Therefore, the optimal elution time was set to 180 min for template molecules.

3.5. Quantitative detection of CEA based on SMIP–IS–SERS immunoassays

In this study, the procedure of CEA detection involves four steps (Fig. 1D). In brief, 3 μL of CEA solutions of different concentrations (100 μg mL^{-1} - 0 pg mL^{-1}) dissolved in PBS (pH 7.4) were added onto each spot of the SMIP arrays and incubated for 20 min in a wet chamber, followed by washing with PBS (pH 7.4) thrice. Then, 3 μL of Au@EB@PDA@Ab NPs was used to specific capture CEA for 3 min. Then, each SMIP array was washed with PBS (pH 7.4) thrice to remove the excess SERS nanotags and dried at room temperature. Finally, the Raman spectra by the CEA SMIP arrays-based SERS were measured using Raman micro-spectroscopy. It is notable that CEA inclusion into MIP will not affect the binding of its antibody. There are two main reasons. First, CEA binding in molecular imprinting relies on covalent reversible binding between a boronic acid ligand and a cis-dihydroxy group of glycoproteins in CEA. However, antibodies recognize antigens via ionic bonds, van der Waals forces, hydrophobic interactions, and hydrogen bonds. Second, the thickness of MIP coating over the CMSM NPs array is about 2.74 nm that is less than the diameter of CEA.

Meanwhile, 3 μL of 10 μg mL^{-1} CEA was incubated in non-imprinting arrays to further evaluate imprinting factor (IF), which was calculated according to the intensity ratio of I_{2024}/I_{2224} for CEA detected on SMIP array and on NIP, using Au@EB@PDA@Ab NPs as SERS nanotags. IF was calculated as followed:

$$IF = \frac{I_M}{I_N} \times 100\%$$

As shown in Fig. 3F, the IF value is 17.65 according to the maximum binding amounts of the SMIP and NIP, thereby confirming the significant binding affinity of the SMIP toward the target glycoprotein. The main reason for the high imprinting factor is that the NIP surface does not form a specific site for recognizing glycoproteins.

In addition, 3 μL of 10 μg mL^{-1} CEA was incubated in the boronic acid-functionalized CMS NPs-coated arrays to evaluate imprinting efficiency (IE). Imprinting efficiency (IE) was calculated as:

$$IF = \frac{I_M}{I_0} \times 100\%$$

where, I_M and I_0 were the Raman signal intensities obtained in SMIP and the boronic acid-functionalized CMS NPs-coated arrays respectively, under the saturated CEA concentration. The higher IE means the better degree of matching between the recognition site and the analyte in SMIP. As shown in Fig. 3D, the IE was calculated to be 30.6%, which is acceptable according to previous report (Tu et al., 2016).

We next applied the novel strategy for quantitative CEA detection. Fig. 4A and B shows the SERS spectra of CEA with different concentrations. It can be obviously found that the SERS spectral intensity of peak at 2024 cm^{-1} gradually decreased associated with decreasing CEA concentration. The result indicated that the number of SERS nanotags was closely related to the concentration of CEA on the SMIP arrays. Then, we plotted the absolute Raman intensity of peak at 2024 cm^{-1} with different concentrations of CEA, and found that there was a linear regression value (R^2) of 0.93646 (Fig. 4C). Further, when plotting the intensity ratio of I_{2024}/I_{2224} with the CEA concentration, we can obtain better linear correlation with a linear regression value (R^2) of 0.98611 (Fig. 4D). In this case, the limit of detection can be achieved at 0.064 pg mL^{-1} with a signal to noise ratio (S/N) of 3 at the detection range of 0.1 pg mL^{-1} - 10 μg mL^{-1} (Zeng et al., 2017). Compared with previous literatures (Table 1), our method has better sensitivity. In the meanwhile, we also chose three kinds interfering substances including AFP, glucose, and BSA to test the specificity of this assay under the same condition (Fig. 3F). These results suggested that the CEA-imprinted arrays exhibited specific performance towards CEA.

These excellent performances can be attributed to following reasons. (1) The Raman reporter we used has a district silent Raman signal locating in the region of 1800–2300 cm^{-1}, which can dramatically

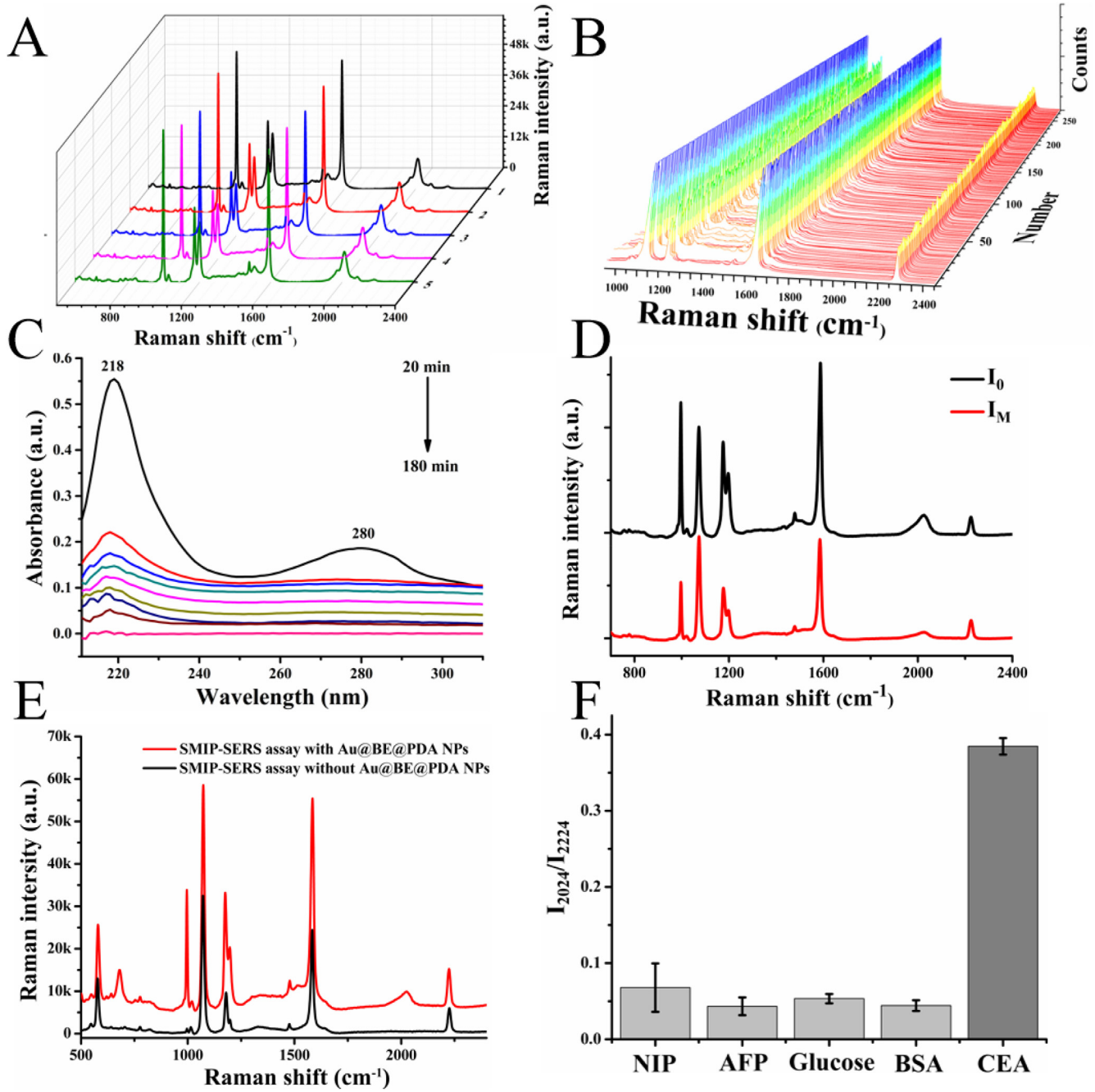

Fig. 3. (A) Signal reproducibility studies of Au@EB@PDA NPs prepared by the one-pot incorporation strategy. The experiments were carried out in five parallel samples. (B) Uniformity of the internal standard of the C≡N signal in the CMSM NPs substrate by scanning 274 Raman spectra over an area of 200 μm, was obtained (RSD = 9.95%). (C) The UV–Vis absorption spectrum of CEA eluent in 20–180 min. (D) Raman spectra on boronic acid-functionalized CMSM NPs arrays and CEA-imprinted CMSM NPs arrays. Sample: 10 μg mL^{-1} CEA dissolved in PBS (pH 7.4). Raman nanotags: Au@EB@PDA@Ab NPs. (E) SMIP-SERS array with Au@EB@PDA@Ab NPs (red line), and SMIP-SERS array without Au@EB@PDA@Ab NPs (black line). (F) Raman spectra on non-imprinted arrays. Sample: 10 μg mL^{-1} CEA. Raman nanotags: Au@EB@PDA@Ab NPs. Cross-reactivity on CEA-imprinted arrays. Sample: 10 μg mL^{-1} AFP, 10 μg mL^{-1} glucose, 10 μg mL^{-1} BSA interfering substance or 10 μg mL^{-1} CEA dissolved in PBS (pH 7.4). Raman nanotags: Au@EB@PDA@Ab NPs. (For interpretation of the references to color in this figure legend, the reader is referred to the Web version of this article.)

avoid the optical noises originating from endogenous molecules at traditional fingerprint region (300-1800 cm^{-1}). (2) Instead of using the single SERS peak, we here employed the intensity ratio based on SERS reporter (C≡C) and IS molecule (C≡N) to indicate the concentrations of CEA. Better linear correlation could be achieved because of the use of this IS molecule, which generated a sharp and stable Raman signal at 2224 cm^{-1} to real-time correct the fluctuating signals of Raman probe and eventually make the results of quantitative detection more stable and accurate. (3) The SERS substrate prepared here can generate plenty of "hot spots" which give rise to great electromagnetic fields due to the effect of localized surface plasmon resonances in nanostructured metals (Kleinman et al., 2013; Shiohara et al., 2014). As shown in Fig. 1, these "hot spots" can exist not only in the gap between core-shell nanospheres in the same layer but also between the upper and the lower layers of nanospheres, leading to a huge enhancement of Raman signals for both SERS reporter and IS molecules. Fig. 3E shows the comparison of SERS signal at 2224 cm^{-1} of IS molecule (C≡N) using SMIP-SERS technology with and without Au@EB@PDA NPs. In addition, we compared the

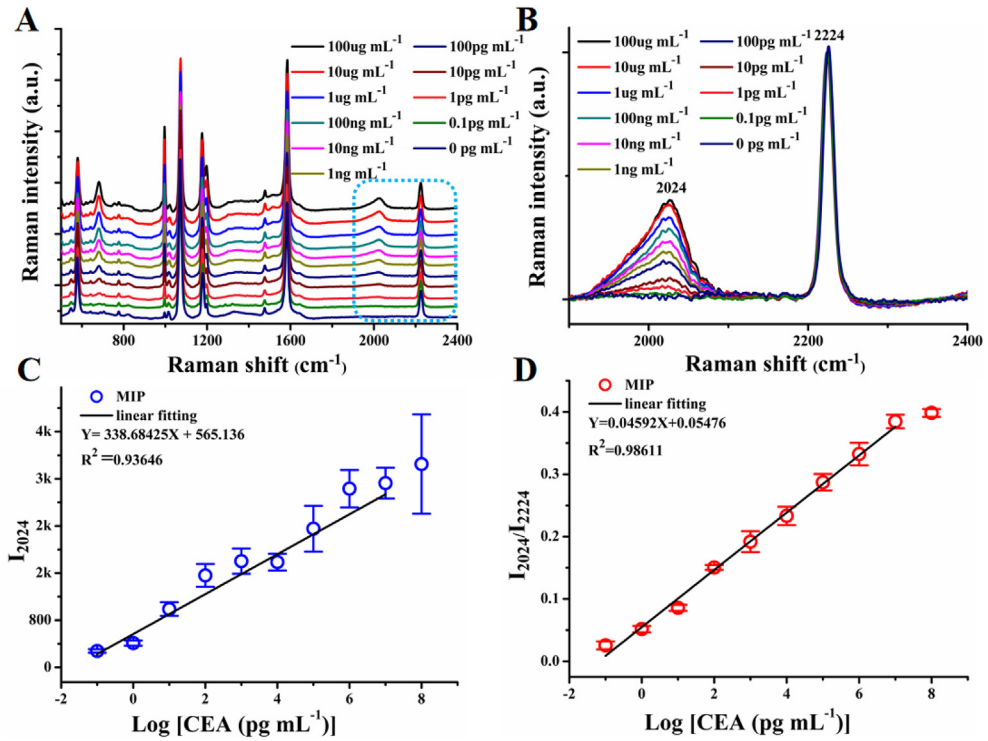

Fig. 4. (A) Raman spectra for CEA at different concentrations (dissolved in PBS) obtained on CEA-SMIP arrays using Au@EB@PDA@Ab NPs as Raman nanotags. (B) This is an enlarged portion of the dotted box in (A). (C) CEA detection logarithmic concentration curves generated by plotting the average intensity at 2024 cm^{-1}. (D) CEA detection logarithmic concentration curves generated by ratio of the peaks at 2024 cm^{-1} and 2224 cm^{-1} (I_{2024}/I_{2224}).

SERS signal of the SMIP arrays without Raman probe (n = 50) and SMIP arrays with Raman probe (n = 50) (Figs. S4B and C). It could be found that this SERS peak was more intense at the presence of Au@EB@PDA NPs layer, which confirmed the enhancement of electromagnetic fields within double nanoparticle layers. This structure will definitely offer excellent amplification for Raman signals of both SERS reporter (C≡C) and IS molecule (C≡N) in this study. (4) Different from the traditional immune-SERS assay (Gao et al., 2018; Lin et al., 2016), this work employs SMIP technology to prepare highly specific recognition sites to capture the CEA via the reversible covalent binding between boronic acids and sugars (Ye et al., 2015), meanwhile, these recognition sites imprinted on the surface of substrate are much more stable than the bare antibody fixed onto the substrate via chemical bonds. Besides, the dynamical interference from external environment can be dramatically avoided by this fabrication method, which improves the efficiency of immune-SERS assay.

3.6. Clinical samples analysis

Due to the great performance shown above, we continued to evaluate the feasibility of this method for CEA detection in real serum samples (Fig. 5). First of all, a serum sample was spiked with different CEA concentrations (C_i) for SERS detection and the pure serum samples' C_0 value was first calculated to be 0.52 pg mL^{-1} according to the linear equation obtained with standard solutions (Y = 0.04592X + 0.05476, R^2 = 0.98611, Fig. 4D). Similarly, we compared the quantitative detection results obtained with and without the correction procedure using IS as shown in Fig. 5C and D. As we expected, better linear correlation with a linear regression value (R^2) of 0.9743 can be achieved when we plotted the intensity ratio of I_{2024}/I_{2224} with the CEA concentration. These preliminarily results suggested our proposed method was also available to indicate the concentration of CEA in serum samples.

Next, we applied this method for direct detection of CEA concentration in unprocessed 7 serum samples. Table 2 summarizes the results obtained by our SMIP-SERS method and traditional ECLIA method with a range from 1.42 to 325 ng mL^{-1}, and the recoveries of CEA range from 98.4 to 106.3%. The results indicated that the accuracy of the proposed SMIP-SERS method was in good agreement with that of the ECLIA. Moreover, the limit detection range (LDR) of our method (from 0.0001 ng mL^{-1} up to 10000 ng mL^{-1} for CEA) was much better than that of the ECLIA kit (LDR from 0.2 to 1000 ng mL^{-1} for CEA). Especially, only 3 μL volume of each sample was required in our method, which was much less than that used in ECLIA. These results strongly suggested the promising potential of this method for clinical CEA-related cancer screening.

4. Conclusions

In this study, a novel biosensor combing SMIP and SERS technologies was developed for quantitative detection of CEA. With the use of surface imprinting approach, highly specific and stable recognition sites were prepared to capture the target of interest. In addition, we designed a special detection platform with double nanoparticles layers where rich “hot spots” were generated to significantly amplify the SERS signals. Different from traditional label-SERS assay, a unique Raman reporter (C≡C) with district silent Raman signal locating in the region of 1800–2300 cm^{-1} was used here to avoid the optical noises originating from endogenous molecules at fingerprint region (300-1800 cm^{-1}). Moreover, we employed an IS molecular (C≡N) to real time correct the fluctuating signals of Raman reporter when performing the quantitative analysis. Due to aforementioned features, the LOD of 0.064 pg mL^{-1} with the detection range of 0.1 pg mL^{-1} - 10 μg mL^{-1} can be achieved by this technology. Excitingly, this technology even showed wonderful performances for CEA detection in real blood samples from cancer patients, demonstrating great potential for biomarkers-based cancer screening. Notably, much effort in the future should be made to address the limitations associated with this biosensor. First, the fabrication procedure should be further simplified through modifying the sensing structure, meanwhile remaining the ultra-high performance. Second, this biosensor can be fabricated with multiple specially-designed probes to simultaneously detect different disease-related biomarkers in a biological sample, which will provide more diagnostic information. Third, we intend to optimize this biosensor to make it suitable for the whole

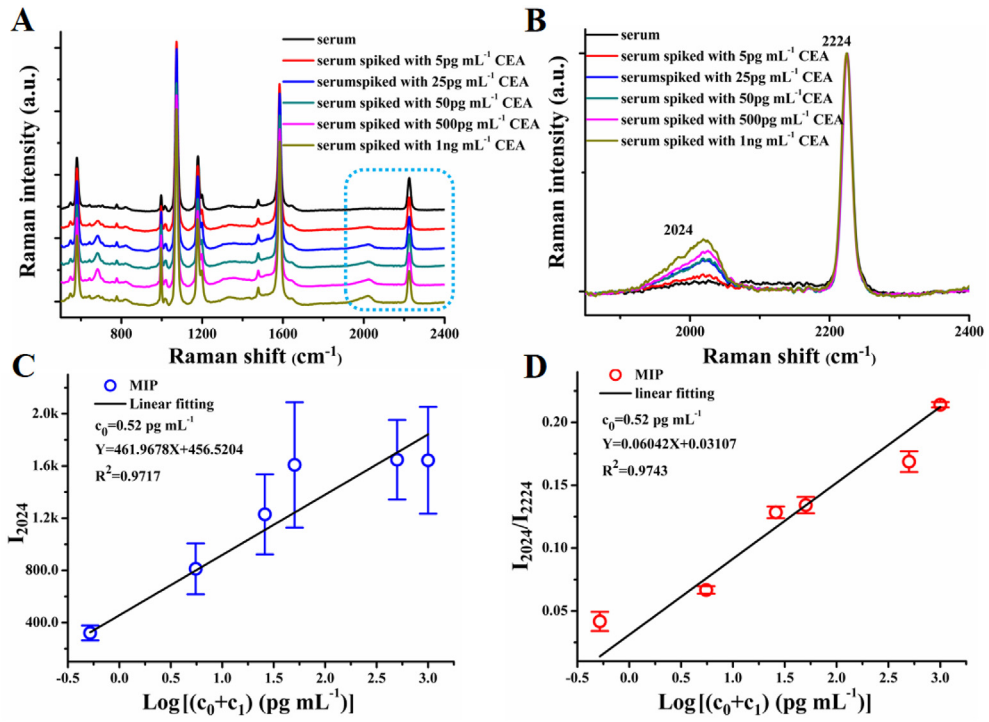

Fig. 5. (A) Raman spectra for CEA at different concentrations (dissolved in serum) obtained on CEA-SMIP arrays using Au@EB@PDA@Ab NPs as Raman nanotags. (B) This is an enlarged portion of the dotted box in (A). (C) Relationship between SERS average intensity at 2024 cm^{-1} and logarithmic concentration of CEA. (D) Relationship between SERS intensity ratio of I_{2024}/I_{2224} and logarithmic concentration of CEA.

blood sample instead of serum sample, which is more suitable and convenient for future clinic use.

CRediT authorship contribution statement

Xueliang Lin: Investigation, Writing - original draft. **Yunyi Wang:** Investigation. **Lingna Wang:** Investigation. **Yudong Lu:** Investigation. **Jin Li:** Formal analysis. **Dechan Lu:** Formal analysis, Methodology, Writing - review & editing. **Ting Zhou:** Formal analysis. **Zufang Huang:** Validation. **Jun Huang:** Investigation. **Huifang Huang:** Resources. **Sufang Qiu:** Resources. **Rong Chen:** Funding acquisition. **Duo Lin:** Methodology, Writing - review & editing. **Shangyuan Feng:** Supervision, Project administration, Funding acquisition.

Declaration of competing interest

The authors declare that they have no known competing financial interests or personal relationships that could have appeared to influence the work reported in this paper.

Acknowledgements

This work was supported by the National Natural Science Foundation of China (No. 61975031, 11974077, 61575043, U1605253, 81741008), the Innovation Team Development Plan by the Ministry of Education of China (No. IRT15R10), the distinguished young researcher of universities of Fujian province and the National Natural Science Foundation of Fujian, China (No. 2017J01499), Special Funds of the Central Government Guiding Local Science and Technology Development (No. 17L3009), Fujian provincial health and family planning research talent training program (No. 2018-CX-13), the Natural Science Foundation of Fujian Province, China (No. 2018J01786).

Appendix A. Supplementary data

Supplementary data to this article can be found online at https://doi.org/10.1016/j.bios.2019.111599.

References

Ahn, B.K., 2017. J. Am. Chem. Soc. 139 (30), 10166–10171.
Alvarez Puebla, R.A., Liz Marzán, L.M., 2010. Small 6 (5), 604–610.
Chen, W., Zheng, R., Baade, P.D., Zhang, S., Zeng, H., Bray, F., Jemal, A., Yu, X.Q., He, J., 2016a. CA: Cancer J. Clin. 66 (2), 115–132.
Chen, Y., Ren, J.-Q., Zhang, X.-G., Wu, D.-Y., Shen, A.-G., Hu, J.-M., 2016b. Anal. Chem. 88 (12), 6115–6119.
Feng, S., Zheng, Z., Xu, Y., Lin, J., Chen, G., Weng, C., Lin, D., Qiu, S., Cheng, M., Huang, Z., 2017. Biosens. Bioelectron. 91, 616–622.
Feng, T., Qiao, X., Wang, H., Sun, Z., Hong, C., 2016. Biosens. Bioelectron. 79, 48–54.
Gao, R., Cheng, Z., Wang, X., Yu, L., Guo, Z., Zhao, G., Choo, J., 2018. Biosens. Bioelectron. 119, 126–133.
Grabar, K.C., Freeman, R.G., Hommer, M.B., Natan, M.J., 1995. Anal. Chem. 67 (4), 735–743.
Han, Q., Wang, R., Xing, B., Zhang, T., Khan, M.S., Wu, D., Wei, Q., 2018. Biosens. Bioelectron. 99, 493–499.
Hanash, S.M., Pitteri, S.J., Faca, V.M., 2008. Nature 452 (7187), 571.
Khang, H., Cho, K., Chong, S., Lee, J.H., 2017. Biosens. Bioelectron. 90, 46–52.
Kleinman, S.L., Frontiera, R.R., Henry, A.-I., Dieringer, J.A., Van Duyne, R.P., 2013. Phys. Chem. Chem. Phys. 15 (1), 21–36.
Kong, K.V., Ho, C.J.H., Gong, T., Lau, W.K.O., Olivo, M., 2014. Biosens. Bioelectron. 56, 186–191.
Konishi, T., Shimada, Y., Hsu, M., Tufts, L., Jimenez-Rodriguez, R., Cercek, A., Yaeger, R., Saltz, L., Smith, J.J., Nash, G.M., 2018. JAMA Oncol. 4 (3), 309–315.
Lee, A., Ma, B., Ng, W.T., Chan, A., 2015. J. Clin. Oncol. 33 (29), 3356–3364.
Lee, H., Dellatore, S.M., Miller, W.M., Messersmith, P.B., 2007. Science 318 (5849), 426–430.
Li, J.-F., Zhang, Y.-J., Ding, S.-Y., Panneerselvam, R., Tian, Z.-Q., 2017. Chem. Rev. 117 (7), 5002–5069.
Li, J., Liu, H., Rong, P., Zhou, W., Gao, X., Liu, D., 2018. Nanoscale 10 (17), 8292–8297.
Lin, D., Gong, T., Qiu, S., Wu, Q., Tseng, C.-Y., Kong, K.V., Chen, G., Chen, R., 2019a. Chem. Commun. 55 (11), 1548–1551.
Lin, X., Wang, L., Lin, H., Lin, D., Lin, J., Liu, X., Qiu, S., Xu, Y., Chen, G., Feng, S., 2019b. J. Biophot. 12 (4), e201800327.
Lin, Y., Xu, G., Wei, F., Zhang, A., Yang, J., Hu, Q., 2016. J. Pharm. Biomed. Anal. 121, 135–140.
Lin, Z., Lv, S., Zhang, K., Tang, D., 2017. J. Mater. Chem. B 5 (4), 826–833.
Liu, R., Zhang, S., Wei, C., Xing, Z., Zhang, S., Zhang, X., 2016. Acc. Chem. Res. 49 (5), 775–783.
Liu, W., Guo, Y., Zhao, M., Li, H., Zhang, Z., 2015. Anal. Chem. 87 (15), 7951–7957.
Lumachi, F., Chiara, G., Tozzoli, R., Re, G.L., Basso, S., 2016. Ann. Oncol. 27 (Suppl. 2), ii10.
Lv, Y., Qin, Y., Svec, F., Tan, T., 2016. Biosens. Bioelectron. 80, 433–441.
Pang, Y., Wang, C., Lu, L., Wang, C., Sun, Z., Xiao, R., 2019. Biosens. Bioelectron. 130, 204–213.
Shen, W., Lin, X., Jiang, C., Li, C., Lin, H., Huang, J., Wang, S., Liu, G., Yan, X., Zhong, Q., 2015. Angew. Chem. Int. Ed. Engl. 54 (25), 7308–7312.
Shiohara, A., Wang, Y., Liz-Marzán, L.M., 2014. J. Photochem. Photobiol. C Photochem.

Rev. 21, 2–25.
Siegel, R.L., Miller, K.D., Jemal, A., 2016. CA: Cancer J. Clin. 66 (1), 7–30.
Tang, L., Li, S., Han, F., Liu, L., Xu, L., Ma, W., Kuang, H., Li, A., Wang, L., Xu, C., 2015. Biosens. Bioelectron. 71, 7–12.
Tu, X., Muhammad, P., Liu, J., Ma, Y., Wang, S., Yin, D., Liu, Z., 2016. Anal. Chem. 88 (24), 12363–12370.
Wang, S., Ye, J., Bie, Z., Liu, Z., 2014. Chem. Sci. 5 (3), 1135–1140.
Wang, Z., Zong, S., Wu, L., Zhu, D., Cui, Y., 2017. Chem. Rev. 117 (12), 7910–7963.
Ye, J., Chen, Y., Liu, Z., 2015. Angew. Chem. Int. Ed. Engl. 53 (39), 10386–10389.
Zeng, H., Agyapong, D.A.Y., Li, C., Zhao, R., Yang, H., Wu, C., Jiang, Y., Liu, Y., 2015a. Sens. Actuators B Chem. 221, 22–27.
Zeng, Y., Pei, J.-J., Wang, L.-H., Shen, A.-G., Hu, J.-M., 2015b. Biosens. Bioelectron. 66, 55–61.
Zeng, Y., Ren, J.-Q., Wang, S.-K., Mai, J.-M., Qu, B., Zhang, Y., Shen, A.-G., Hu, J.-M., 2017. ACS Appl. Mater. Interfaces 9 (35), 29547–29553.
Zong, C., Xu, M., Xu, L.J., Wei, T., Ma, X., Zheng, X.S., Hu, R., Ren, B., 2018. Chem. Rev. 4946–4980.